

Complete description of two-photon ($1+1'$) ionization of NO deduced from rotationally resolved photoelectron angular distributions

David J. Leahy, Katharine L. Reid, and Richard N. Zare
Chemistry Department, Stanford University, Stanford, California 94305

(Received 18 January 1991; accepted 29 March 1991)

Time-of-flight photoelectron spectroscopy has been used to record energy-resolved photoelectron angular distributions (PADs) following ($1+1'$) resonance-enhanced multiphoton ionization (REMPI) of NO via the $v_i = 1, N_i = 22$ rovibrational level of the $A^2\Sigma^+$ state. The PADs corresponding to single rotational states of the resulting molecular ion show a strong dependence on the change in ion core rotation $\Delta N (\equiv N^+ - N_i)$ and also on the angle between the linear polarization vectors of the two light beams. Broken reflection symmetry [$I(\theta, \phi) \neq I(-\theta, \phi)$] is observed when the polarization vectors of the two light beams form an angle of 54.7° . A fit to the PADs provides a complete description of this molecular photoionization, namely, the magnitudes and phases of the radial dipole matrix elements that connect the intermediate state to the $|\mathcal{M}\rangle$ photoelectron partial waves (Refs. 1 and 2). This information is then used to predict unobserved quantities, such as ion angular momentum alignment and the full three-dimensional form of the PADs.

INTRODUCTION

Molecular photoionization can be considered a "reactive collision" between a neutral molecule and a photon, yielding a molecular ion and a photoelectron. In fact, this process is one of the simplest molecular scattering phenomena. Because of the tiny mass of the photoelectron, the scattering process can be described by just a few partial waves that correspond to different values of photoelectron orbital angular momentum l and its projection λ on the internuclear axis. Another useful consequence of the large ratio between the masses of the ion and electron is that virtually all of the available kinetic energy from the photofragmentation goes to the photoelectron; the specificity of this energy transfer facilitates the determination of ion internal state distributions and scattering differential cross sections in one measurement. Taken together, these facts indicate that the observation of *ion rotational-level-resolved* photoelectron angular distributions (PADs) following resonance-enhanced multiphoton ionization (REMPI) can provide a quantitative probe of the photoionization dynamics.^{3,4} Indeed, information deduced from the shapes and intensities of these PADs can provide a complete quantum mechanical description of the system state resulting from the photoionization:^{1,5} thus, the observation of these PADs constitutes a perfect experiment.

Consider ($1+1'$) REMPI of an isotropic distribution of atoms or molecules by two linearly polarized photons with an arbitrary angle Θ_T between their polarization vectors. We choose the laboratory frame such that the Z axis is along the polarization vector of the ionizing light beam (Fig. 1). The resulting PADs take the general form

$$I(\theta, \phi) = \beta_{00} Y_{00}(\theta, \phi) + \sum_{L=2,4} \sum_{M=-2}^{+2} \beta_{LM} Y_{LM}(\theta, \phi), \quad (1)$$

where θ and ϕ are the polar and azimuthal angles measured about the Z axis. The expansion in the spherical harmonics $Y_{LM}(\theta, \phi)$ is truncated at $L \leq 4$ because the only anisotropy introduced to the system is from the absorption of two linearly polarized photons.³ In addition, L must be even because photoelectron intensity that results from ionization of an isotropic ensemble with linearly polarized light must have inversion symmetry. In the special case where the two linear polarization vectors are parallel ($\Theta_T = 0^\circ$), cylindrical symmetry is present, and the consequence is that $M = 0$ only. In general, however, for arbitrary Θ_T , contributions to $I(\theta, \phi)$ arise from the $M \neq 0$ terms.² In particular, $M = \pm 1$ terms break reflection symmetry in the PAD [$I(\theta, \phi) \neq I(-\theta, \phi)$]. Changing the angle between the polarization vectors (Θ_T) allows a more complete probing of the aligned intermediate state ensemble by the electric field of the ionizing light. For example, for resonant excitation via a Q branch, the $\Theta_T = 0^\circ$ geometry probes preferentially perpendicular to the internuclear axis. For $\Theta_T = 90^\circ$, on the other hand, the ionizing electric vector often lies parallel to the internuclear axis.

In this paper we present observations of PADs that extend the studies of Reilly and co-workers⁴ and of Allendorf *et al.*¹ on the ($1+1'$) REMPI system $\text{NO } X^2\Pi \rightarrow \text{NO } A^2\Sigma^+ \rightarrow \text{NO}^+ X^1\Sigma^+ + e^-$. As in the previous studies, we prepare a single rovibrational level of the $A^2\Sigma^+$ state with the absorption of a single, linearly polarized photon; here we excite $v_i = 1$ as opposed to $v_i = 0$ in Refs. 1 and 4. A second photon, with independent frequency and polarization, causes the ionization. The PADs are measured by performing field-free time-of-flight (TOF) photoelectron energy analyses at a set of angles θ for a given Θ_T . Through the generation of slow photoelectrons (132.6–187.2 meV) we can resolve the energy spacing between the rotational levels of the ion in each photoelectron TOF spectrum.

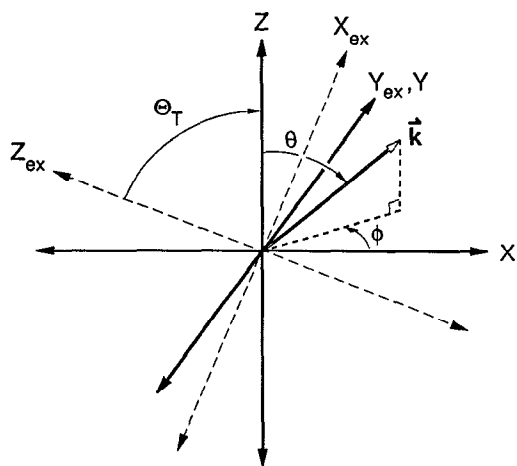


FIG. 1. Illustration of the axes and angles referred to in the text. The detector lies in the XZ plane ($\phi = 0^\circ$), and the light beams propagate along the Y axis.

The resulting “rotationally resolved” PADs are used in a fitting process to determine electric dipole matrix elements (both magnitude and phase) that connect the intermediate $A^2\Sigma^+$ state to the few accessible $|l\rangle$ photoelectron continua. These results are compared with earlier results⁵ and *ab initio* calculations.⁶ The dipole matrix elements represent a complete description of the photoionization process, i.e., this information allows the prediction of all experimentally unobserved quantities, such as molecular ion angular momentum alignment and fully three-dimensional PADs.

EXPERIMENT

The experimental apparatus is described elsewhere¹ in detail and shown schematically in Fig. 2. Its essence is simply a magnetically shielded field-free flight tube. The photoelectrons are produced at the intersection of a molecular beam with two counterpropagating pulsed laser beams, at a distance of 51 cm from an electron detector. Photoelectron

flight-time distributions are accumulated over many laser pulses for each of several laser polarization geometries.

The apparatus consists of two main parts, an ionization chamber and a source chamber. The flight tube, which takes up most of the ionization chamber, consists of two concentric cylinders of mu-metal that are equipped with electron baffles and coated with colloidal graphite (Aerodag, Acheson). The flight tube has no applied fields, and static magnetic (< 5 mG) and electric fields have been minimized carefully. A differentially pumped source chamber contains a pulsed nozzle (General Valve) with a 0.8 mm orifice. Resistive heating to 70°C helps counteract the cooling of the gas expansion. The nozzle is backed with 1.3 atm of 99% pure NO (Matheson CP) and directed into a skimmer with a 0.3 mm pinhole. Both the ionization chamber and the source chamber are evacuated with turbomolecular pumps; during the experiment, their pressures were 8×10^{-8} and 8×10^{-5} Torr, respectively.

The two colors, λ_1 and λ_2 , originated from Nd:YAG-pumped pulsed dye lasers (DCR-1 and PDL-1, GCR-3 and PDL-3; Spectra-Physics) operating at a repetition rate of 10 Hz. The excitation color λ_1 (214.35 nm) was generated by focusing the frequency-doubled output of the PDL-3 dye laser in a hydrogen Raman cell and selecting the third anti-Stokes order. This beam, resonant with the $P_{21} + Q_1$ (22.5) transition terminating on the $v_i = 1, N_i = 22$ level of the NO $A^2\Sigma^+$ state, was attenuated to about $1 \mu\text{J}/\text{pulse}$. The ionization color λ_2 (313.84 nm) was produced by frequency-doubling the output of the PDL-1 dye laser, giving an ultraviolet linewidth of 0.6 cm^{-1} ; $400 \mu\text{J}/\text{pulse}$ was admitted into the chamber. The two counterpropagating laser beams entered the ionization chamber at right angles to both the molecular beam and the detection axis (see Figs. 1 and 2). Both laser beams were passed through zeroth-order quartz waveplates (Special Optics) mounted on stepper-motor-driven rotation stages, which allowed independently rotatable polarizations. The outputs of both lasers were focused with a 500 mm lens; the ionization beam was focused quite loosely. Under these

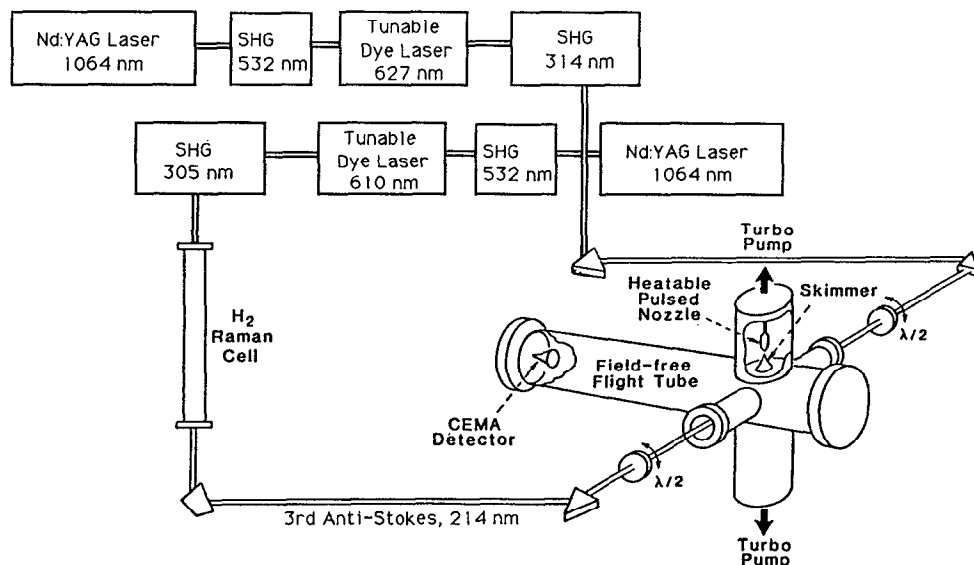


FIG. 2. Schematic of the experimental apparatus.

focusing conditions, no saturation effects could be observed on varying the intensity of each of the two colors.

To obtain high resolution of the photoelectron kinetic energy, long flight times were needed, with correspondingly low photoelectron kinetic energies (100 to 300 meV). At these photoelectron energies, careful minimization of stray electric and magnetic fields was crucial. Ion production was limited to roughly 500 ions per laser pulse to avoid space-charge broadening of the time-of-flight spectra. The photoelectrons were observed with a 4 cm CEMA detector; the flight region was shielded from the detector's positive high-voltage potential by two layers of grounded conducting mesh. No detection efficiency discrimination could be discerned with respect to the velocity of the photoelectrons. With our low collection efficiency (the CEMA subtends a solid angle of 0.005 str), a maximum of one photoelectron per ten laser shots was observed. The flight times were measured with a time-to-amplitude converter (Model 467, Ortec) and recorded with a personal computer (IBM XT). Because of this detection scheme, at most one photoelectron flight time could be measured for each laser pulse; for laser shots that sent more than one photoelectron into the detector, only the first was observed. Signals that arrived later in the spectra were multiplied by a factor to compensate for the statistically indicated quantity of unobserved events.⁷ These corrections were few because multielectron events occurred no more frequently than one per one hundred laser shots. The time-of-flight spectra show clearly resolved peaks corresponding to the rotational levels of the molecular ion (see Fig. 3). The relative energy resolution was 2–3 meV FWHM, more than sufficient to resolve the 10 meV spacing between neighboring rotational levels of NO⁺ for $N^+ = 22$. This energy resolution is an improvement over that reported in Ref. 1 because of the suppression of scattered photoelectrons by a baffle inserted at the halfway point of the flight tube. The assignment of the observed peaks to

ion rotational states was made in accordance with the expected symmetry of the PADs.

A typical angular distribution consisted of 40 000 laser shots per waveplate position, i.e., per detection angle θ , and included 12 angles spanning two quadrants. Our experiments were performed with four different angles Θ_T held between the two polarization vectors: $\Theta_T = 0^\circ$, $\Theta_T = \pm 54.7^\circ$, and $\Theta_T = 90^\circ$. A small number of background electrons arose from scattered 214 nm radiation and from scattered signal photoelectrons. The signal followed binomial statistics, giving statistical error bars approximately equal to the square root of the number of events. For all but the most intense signals, this uncertainty accounted for virtually all of the error in the data.

The ionization color ($\lambda_2 = 313.84$ nm) was chosen so as to give slow (≈ 165 meV) photoelectrons from the formation of NO⁺ $X^1\Sigma^+(v^+ = 1, J^+ = N^+ = 20-24)$. Extremely few photoelectrons corresponding to $\Delta N = \pm 3$ ($\Delta N \equiv N^+ - N_i$) transitions were observed, and none for $|\Delta N| \geq 4$. Virtually no signal was observed that corresponded to the formation of the only other energetically accessible ion vibrational state, $v^+ = 0$; nor was there appreciable ionization by the excitation laser λ_1 .

RESULTS AND ANALYSIS

For the $(1 + 1')$ REMPI process, the symmetry of the photoelectron angular distribution as measured in the laboratory frame depends strongly on the geometry of the linear polarization vectors (i.e., on Θ_T). When $\Theta_T = 0^\circ$, the excitation-ionization process has cylindrical symmetry and a center of inversion (i.e., $D_{\infty h}$); therefore, the photoelectron intensity resulting from an isotropic sample must have the same symmetry. In this case, the PADs are simply described by

$$I(\theta, \phi) = \beta_{00} Y_{00}(\theta, \phi) + \beta_{20} Y_{20}(\theta, \phi) + \beta_{40} Y_{40}(\theta, \phi). \quad (2)$$

Here, β_{00} describes the angle-integrated total cross section of the PAD, and β_{20} and β_{40} dictate the form of the angular dependence. Note that $Y_{00}(\theta, \phi)$ has no dependence on θ or ϕ , while the $Y_{L0}(\theta, \phi)$ with $L > 0$ depend only on θ . These facts make the value of Eq. (2) independent of ϕ (cylindrically symmetric). In addition, since L is always even, the PAD has inversion symmetry [$I(\theta, \phi) = I(\pi - \theta, \phi + \pi)$]. This inversion symmetry is present for all of the PADs that we discuss in this paper. Polar plots of the data recorded at $\Theta_T = 0^\circ$ are presented in Fig. 4, along with the plots of the fits to Eq. (2). The results of the fit are shown in Table I.

When $\Theta_T = 90^\circ$, another special case arises. The photoelectron intensity has D_{2h} symmetry and can be written as

$$I(\theta, \phi) = \beta_{00} Y_{00}(\theta, \phi) + \beta_{20} Y_{20}(\theta, \phi) + \beta_{40} Y_{40}(\theta, \phi) + 2[\beta_{22} Y_{22}(\theta, 0^\circ) + \beta_{42} Y_{42}(\theta, 0^\circ)] \cos(2\phi). \quad (3)$$

The $Y_{L\pm 2}(\theta, \phi = 0^\circ)$ are linearly dependent on the $Y_{L0}(\theta, \phi = 0^\circ)$. Because we observe photoelectron intensity only in the $\phi = 0^\circ$ (XZ) plane (see Fig. 1), we cannot

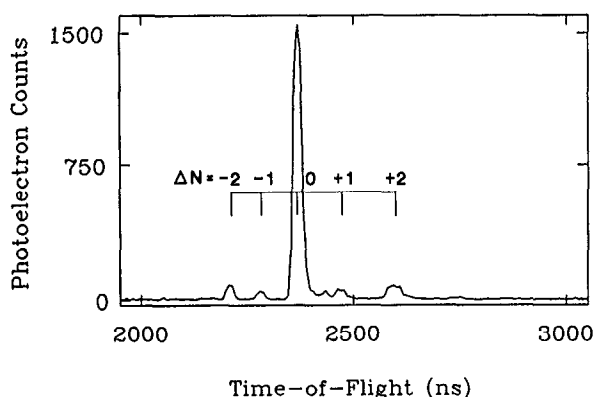


FIG. 3. Photoelectron time-of-flight spectrum for $(1 + 1')$ REMPI of NO via the $P_{21} + Q_1(22.5)$ transition to the $A^2\Sigma^+(v_i = 1, N_i = 22)$ level, with $\Theta_T = 0^\circ$. The small peak between the $\Delta N = 0$ and $\Delta N = +1$ peaks arose from $\Delta N = 0$ electrons scattered from the walls of the flight tube; this signal was excluded from the peak integrations.

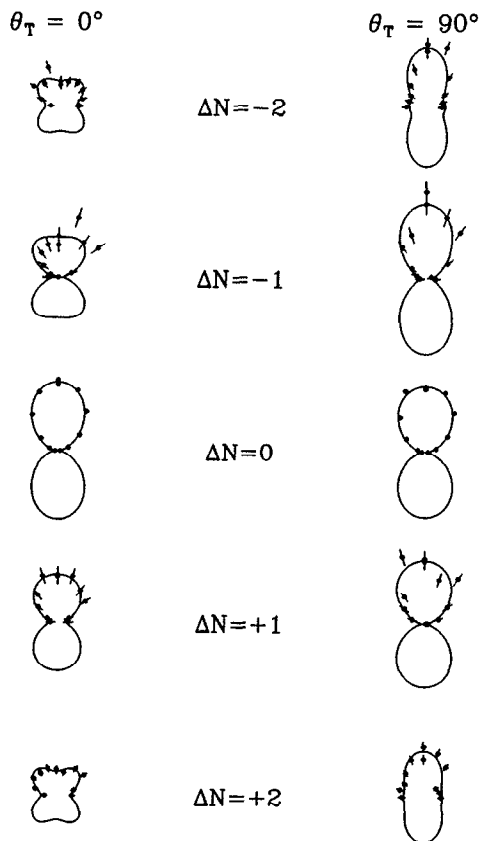


FIG. 4. Polar plots of the PADs for $\Theta_T = 0^\circ$ and $\Theta_T = 90^\circ$, where the linear polarization vector of the ionizing radiation is along the vertical direction. The bars on the data represent 1σ uncertainties. The solid lines are results of the fit to Eqs. (2) and (4) (see Table I). For ease of comparison, all plots have been drawn with β_{00} set to unity.

uniquely determine all of the β_{LM} coefficients in Eq. (3). Therefore we fit our data to the β'_{LM} coefficients of Eq. (4),

$$I(\theta, \phi = 0^\circ) = \beta'_{00} Y_{00}(\theta, 0^\circ) + \beta'_{20} Y_{20}(\theta, 0^\circ) + \beta'_{40} Y_{40}(\theta, 0^\circ). \quad (4)$$

Because the ϕ dependence of the PADs is unobserved, the

resulting β'_{00} of our fits [unlike the β_{00} of Eq. (3)] do not represent angle-integrated cross sections. Polar plots of our data for $\Theta_T = 90^\circ$ are presented in Fig. 4 and the results of the fit in Table I.

Finally, we discuss PADs for arbitrary Θ_T ($\neq 0^\circ$ and $\neq 90^\circ$). Here, the PADs have C_{2h} symmetry, which consists of an inversion center, a C_2 axis along the Y axis (see Fig. 1), and a σ_h plane (XZ). The fully three-dimensional form of the intensity is

$$I(\theta, \phi) = \beta_{00} Y_{00}(\theta, \phi) + \beta_{20} Y_{20}(\theta, \phi) + \beta_{40} Y_{40}(\theta, \phi) + 2[\beta_{21} Y_{21}(\theta, 0^\circ) + \beta_{41} Y_{41}(\theta, 0^\circ)] \cos(\phi) + 2[\beta_{22} Y_{22}(\theta, 0^\circ) + \beta_{42} Y_{42}(\theta, 0^\circ)] \cos(2\phi). \quad (5)$$

The intensity in the XZ plane goes as

$$I(\theta, \phi = 0^\circ) = \beta'_{00} Y_{00}(\theta, 0^\circ) + \beta'_{20} Y_{20}(\theta, 0^\circ) + \beta'_{40} Y_{40}(\theta, 0^\circ) + 2[\beta_{21} Y_{21}(\theta, 0^\circ) + \beta_{41} Y_{41}(\theta, 0^\circ)]. \quad (6)$$

The contributions to Eqs. (5) and (6) of functions that are odd in θ [namely, the $Y_{L1}(\theta, \phi)$] break the reflection symmetry σ_v that was present in the $D_{\infty h}$ and D_{2h} groups. This break is strikingly apparent in the PADs shown in Fig. 5, which were recorded at $\Theta_T = \pm 54.7^\circ$. Clearly, $I(\theta, \phi) \neq I(-\theta, \phi)$. Results of the fits of these PADs to Eq. (6) are shown in Table II. Again, because of the unobserved ϕ dependence, the β'_{00} do not represent angle-integrated cross sections for arbitrary Θ_T .

The intermediate state $A^2\Sigma^+$ cannot be prepared via a pure Q branch with our present laser system because the splitting between spin-rotation doublets is very small. The $P_{21} + Q_1$ branch was chosen because the ratio of $P:Q$ is about 1:8 when $J_g = 22.5$. This predominantly parallel transition gives the largest degree of angular momentum alignment attainable for our system of study. This high degree of alignment facilitates preferential probing of parallel or perpendicular ionization moments by choice of Θ_T . As pre-

TABLE I. Results of fitting the β_{LM} to experimental PADs for $(1 + 1')$ REMPI via the $P_{21} + Q_1$ (22.5) transition to the $A^2\Sigma^+$ ($v_i = 1, N_i = 22$) level. Equation (2) was used for the $\Theta_T = 0^\circ$ data, and Eq. (4) for $\Theta_T = 90^\circ$. To facilitate the comparison of the shapes of the PADs, the β_{LM} ($L > 0$) have been divided by β_{00} for each combination of ΔN and Θ_T . The β_{00} here and in Table II have been normalized such that $\beta_{00} \equiv 100$ for $\Delta N = 0$, $\Theta_T = 0^\circ$. The results of the fit are shown pictorially, with the experimental data, in Fig. 4. The values in parentheses represent 1σ uncertainties. The reduced χ^2 values for each fit are also shown.

Θ_T	β_{LM}	ΔN				
		-2	-1	0	+1	+2
0°	β_{00}	6.1(4)	2.9(4)	$\equiv 100$	4.36(21)	12.1(5)
	β_{20}	0.20(5)	0.57(12)	0.806(24)	0.54(4)	0.20(3)
	β_{40}	-0.14(4)	-0.17(10)	0.010(23)	-0.06(4)	-0.01(3)
	χ^2	1.140	2.105	5.150	0.138	0.890
	β'_{00}	7.3(5)	4.4(4)	105(3)	5.9(6)	12.1(8)
90°	β'_{20}	0.41(6)	0.79(9)	0.782(23)	0.82(9)	0.28(6)
	β'_{40}	0.16(6)	0.12(8)	-0.008(23)	-0.08(7)	0.09(5)
	χ^2	1.264	1.356	4.926	2.016	1.964

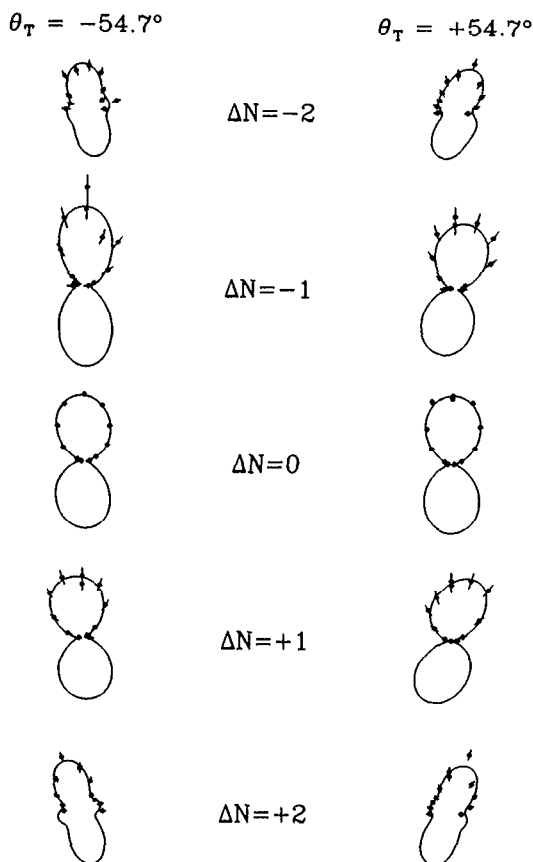


FIG. 5. Polar plots of the PADs for $\Theta_T = \pm 54.7^\circ$. The bars on the data represent 1σ uncertainties. The solid lines are results of the fit to Eq. (6) (see Table II). For ease of comparison, all plots have been drawn with β_{00} set to unity.

viously observed,¹ the PADs depend strongly on the value of ΔN as well as the excitation-ionization geometry (i.e., Θ_T). In fact, the PADs with $\Theta_T = 0^\circ$ and $\Theta_T = 90^\circ$ are quite similar to those reported in Ref. 1 for the $P_{21} + Q_1(25.5)$ transition via $v_i = 0$ of the $A^2\Sigma^+$ state. This similarity suggests

TABLE II. Results of fitting the β_{LM} , using Eq. (6), to experimental PADs for $(1 + 1')$ REMPI via the $P_{21} + Q_1(22.5)$ transition to the $A^2\Sigma^+$ ($v_i = 1, N_i = 22$) level for $\Theta_T = \pm 54.7^\circ$. The β_{LM} ($L > 0$) have been divided by β_{00} for each combination of ΔN and Θ_T . The results of the fit are shown pictorially, with the experimental data, in Fig. 5. The values in parentheses represent 1σ uncertainties. The reduced χ^2 values for each fit are also shown.

Θ_T	β_{LM}	ΔN				
		-2	-1	0	+1	+2
-54.7°	β'_{00}	8.1(5)	3.8(4)	107(3)	6.1(3)	13.2(5)
	β'_{20}	0.25(5)	0.79(10)	0.763(25)	0.71(4)	0.29(4)
	β'_{40}	0.08(5)	0.14(9)	-0.009(24)	-0.04(4)	0.07(3)
	β_{21}	0.09(6)	-0.06(11)	-0.06(3)	0.23(5)	0.17(4)
	β_{41}	0.11(7)	0.07(12)	0.07(3)	-0.01(5)	0.20(5)
	χ^2	1.182	1.462	5.502	0.490	0.927
$+54.7^\circ$	β'_{00}	7.8(4)	4.8(3)	107(3)	5.31(23)	11.9(8)
	β'_{20}	0.32(4)	0.71(5)	0.800(20)	0.75(4)	0.31(5)
	β'_{40}	-0.02(4)	0.00(5)	-0.005(22)	-0.11(3)	0.01(5)
	β_{21}	-0.13(6)	-0.31(6)	-0.02(3)	-0.28(5)	-0.24(7)
	β_{41}	-0.12(6)	-0.02(6)	0.00(3)	-0.10(5)	-0.18(7)
	χ^2	0.991	0.670	4.718	0.441	2.090

that the PADs are not very sensitive to the rovibrational level of the intermediate state.

An important feature of the data is shown in Table II for $\Theta_T = \pm 54.7^\circ$. Like $\Theta_T = 0^\circ$ and $\Theta_T = 90^\circ$, this excitation-ionization geometry represents a special case: there is no population alignment of the intermediate state (i.e., the M_{N_i} sublevels of the intermediate state rotational level N_i have equal populations) in the frame of the ionization laser. In other words, the state multipole $T(2,0)$ (Ref. 8) of the angular momentum tensor is zero. However, since the $T(2, \pm 1)$ and $T(2, \pm 2)$ state multipoles of the intermediate state are nonzero,² the signature of the excitation laser continues to appear in the PADs in the form of a complicated θ and ϕ dependence of the intensity. The magnitudes of the $T(2, \pm 1)$ (and the corresponding degree of broken symmetry in θ) are maximized for $\Theta_T = 45^\circ$; however, we chose to study $\Theta_T = \pm 54.7^\circ$ to demonstrate the importance of the $T(2, Q \neq 0)$ multipoles when all of the M_{N_i} sublevels are equally populated. With this geometry, we have shown that the β_{40} coefficient of Eq. (5) is zero;² our β'_{40} fit results actually reflect the presence of the omitted $\beta_{4\pm 2}$ terms of Eq. (6). Finally, note that the degree of broken symmetry in θ for arbitrary Θ_T is maximized in the $\phi = 0^\circ$ plane.

In Eq. (14) of the preceding paper² the photoelectron intensity for given values of Θ_T and N^+ was shown to be related to radial dipole transition matrix elements as follows:

$$I(\theta, \phi) = \sum_{\Pi'} \sum_{\lambda\lambda'} \sum_{m_i m'_i} \gamma_{N^+ l \lambda m_i l' \lambda' m'_i}(\Theta_T) Y_{lm_i}(\theta, \phi) \times Y_{l'm'_i}^*(\theta, \phi) r_{l\lambda} r_{l'\lambda'} \cos(\eta_{l\lambda} - \eta_{l'\lambda'}). \quad (7)$$

Here $l\lambda$ and $l'\lambda'$ denote interfering photoelectron partial waves, $r_{l\lambda}$ and $\eta_{l\lambda}$ represent the magnitude and phase of the electric dipole matrix element connecting the intermediate state to the $l\lambda$ partial wave, and the $\gamma_{N^+ l \lambda m_i l' \lambda' m'_i}(\Theta_T)$ coefficients contain purely geometric factors. By performing the sum over m_i and m'_i to simplify Eq. (7), we obtain

$$I(\theta, \phi) = \sum_{l'} \sum_{\lambda \lambda'} a_{N+l'l\lambda'}(\Theta_T; \theta, \phi) r_{l\lambda} r_{l'\lambda'} \times \cos(\eta_{l\lambda} - \eta_{l'\lambda'}), \quad (8a)$$

where

$$a_{N+l'l\lambda'}(\Theta_T; \theta, \phi) = \sum_{m_l m_l'} \gamma_{N+l'l m_l m_l'}(\Theta_T) \times Y_{l m_l}(\theta, \phi) Y_{l' m_l'}^*(\theta, \phi). \quad (8b)$$

The data presented in Figs. 4 and 5 can be inserted into a system of simultaneous equations of the form of Eq. (8a). The parameters $r_{l\lambda}$ and $\eta_{l\lambda}$ can then be adjusted to give the best overall fit.

One difficulty of such a fit is that in this system of equations, the parameters $r_{l\lambda}$ are highly correlated; this problem contributes to artificially high uncertainties in the fit. To partially circumvent this, we recast these parameters into a much less correlated form,¹

$$F_l \equiv r_{l\sigma}^2 + 2r_{l\pi}^2 \quad (9a)$$

and

$$\Gamma_l \equiv r_{l\sigma}^2 / (r_{l\sigma}^2 + 2r_{l\pi}^2). \quad (9b)$$

The F_l represent the relative cross sections of each of the l continua, and Γ_l describes the degree of parallel character of the l -wave cross section. Unlike in Ref. 1, no overall normalization is applied to the F_l . Using these parameters we have performed a fit using the Levenberg-Marquadt modified least-squares method.^{9,10} Our partial wave expansion was cut off at $l = 3$. This cutoff is justified primarily by the fact that the small mass of the photoelectron creates a large centrifugal barrier that allows only a few partial waves to escape. Additionally, the observed rotationally resolved PADs (only $|\Delta N| < 2$ branches held significant intensity) do not provide any evidence for the presence of waves with $l > 3$.

The fitting was further facilitated by the selection rule $\Delta N + l = \text{odd}$, which is applicable because both the intermediate NO $A^2\Sigma^+$ state and the ion NO⁺ $X^1\Sigma^+$ state have Σ symmetry.^{11,12} Thus, the $\Delta N = 0, \pm 2$ ionizing transitions involve only odd l partial waves (p, f), while the $\Delta N = \pm 1$ transitions yield only even l waves (s, d). Owing to this simplification, the fit could be decomposed into two independent parts: the even l fit, with parameters $F_s, F_d, \Gamma_d, \eta_{s\sigma}, \eta_{d\sigma},$ and $\eta_{d\pi}$; and the odd l fit, with parameters $F_p, F_f, \Gamma_p, \Gamma_f, \eta_{p\sigma}, \eta_{p\pi}, \eta_{f\sigma},$ and $\eta_{f\pi}$. In each half-fit, we were free to choose one of the phase shifts arbitrarily, since the PADs are sensitive only to the relative phases of interfering waves [see Eq. (8a)]. Thus we defined $\eta_{s\sigma} \equiv \eta_{p\sigma} \equiv 0$. Note that this experiment yields no information about the relative phases between even and odd partial waves. Despite the division of the fitting procedure, the F_l parameters for even and odd l retain their correct relative magnitudes.

The results of the fit, shown in Table III, were unique; no other set of parameters was observed to give as satisfactory a fit. The rotationally resolved PADs proved to be quite sensitive to F_l and less sensitive to the orientation of the dipole moment with respect to the molecular axis (Γ_l). Finally, Figs. 6 and 7 show the model PADs predicted by the fit results [via Eq. (8a)] along with the experimental data.

TABLE III. Parameters resulting from the fit of Eq. (8a) to $\Theta_T = 0^\circ$, $\Theta_T = \pm 54.7^\circ$, and $\Theta_T = 90^\circ$ data for $(1 + 1')$ REMPI of NO via $A^2\Sigma^+(v_i = 0)P_{21} + Q_1(25.5)$, and $(v_i = 1)P_{21} + Q_1(22.5)$. The F_l were normalized to sum to unity. Also shown are the results of the *ab initio* calculation of Rudolph and McKoy (Ref. 6). The values in parentheses represent 1σ uncertainties.

Parameter	Fit (Ref. 5) $v_i = 0$	Fit $v_i = 1$	<i>ab initio</i> (Ref. 6)
F_s	0.048(6)	0.038(4)	0.025
F_p	0.714(10)	0.689(7)	0.655
F_d	0.025(6)	0.042(3)	0.050
F_f	0.212(7)	0.231(6)	0.273
Γ_p	0.368(40)	0.338(31)	0.119
Γ_d	0.54(11)	0.68(11)	0.984
Γ_f	0.314(70)	0.542(61)	0.471
$\delta_{p\sigma - p\pi}$	12.7°(2.3)	9.2°(1.2)	9.8°
$\delta_{d\sigma - d\pi}$	52.7°(8.9)	12°(25)	93.3°
$\delta_{f\sigma - f\pi}$	14°(13)	-2°(29)	1.6°
$\delta_{s\sigma - d\sigma}$	1°(22)	-30°(16)	6.3°
$\delta_{p\sigma - f\sigma}$	124.3°(7.4)	94°(21)	103.7°

DISCUSSION

The dynamics of atomic or molecular photoionization depend on the nature of the electronic wave function of the neutral species and on the potential exerted by the newly formed ion on the departing photoelectron. For atomic pho-

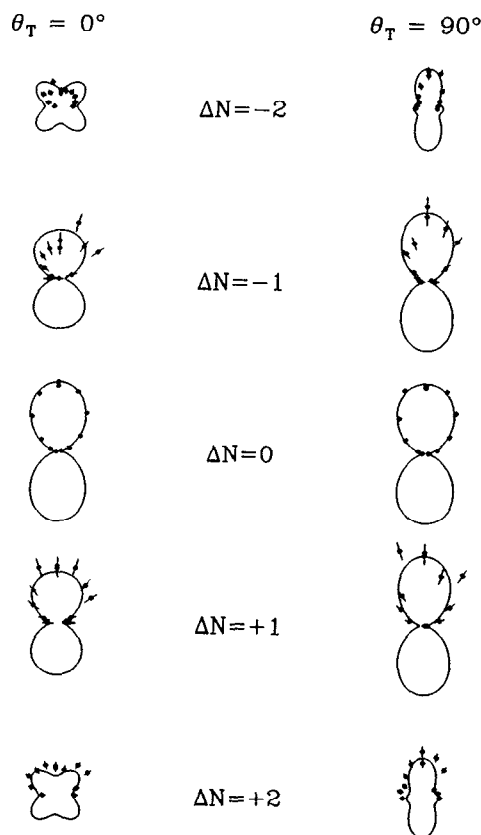


FIG. 6. Polar plots of the calculated PADs for $\Theta_T = 0^\circ$ and $\Theta_T = 90^\circ$, using the parameters of the result of the fit, listed in Table III. The plots also show the experimental data, scaled to the predicted intensities.

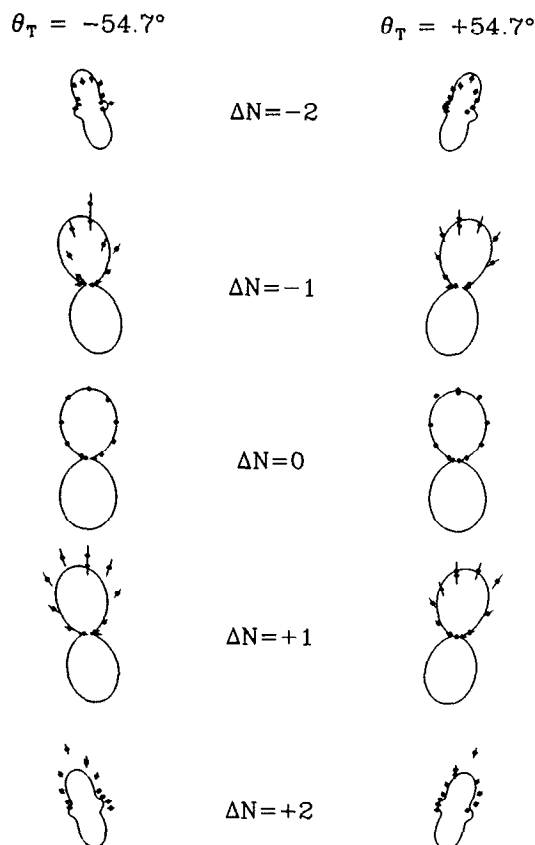


FIG. 7. Polar plots of the calculated PADs for $\Theta_r = \pm 54.7^\circ$, using the parameters of the result of the fit, listed in Table III. The plots also show the experimental data, scaled to the predicted intensities.

toionization, the presence of spherical symmetry and the lack of internal states sharply reduce the number of open photoionization channels. Even for the simplest diatomic molecules, on the other hand, the scattering l channels are split into $(2l + 1)|l\rangle$ subchannels, and nuclear degrees of freedom (vibration and rotation) increase the number of system states accessible in the fragmentation. Although this process is far more complicated than atomic photoionization, it also yields more observables. This gain in observables is especially useful when the role of molecular rotation in the photoionization is considered. In our work, we exploit this structural richness in two ways: we use angular momentum alignment to preferentially probe parallel and perpendicular ionization channels (through varying the excitation-ionization geometry), and we resolve molecular ion rotational levels in the photoelectron spectra to gain specific information about all possible paths of angular momenta transfer. Because of these advantages, we can generate a complete description of the $(1 + 1')$ REMPI system $\text{NO } X^2\Pi(v_g = 0, J_g = 22.5) \rightarrow \text{NO } A^2\Sigma^+(v_i = 1, N_i = 22) \rightarrow \text{NO}^+ X^1\Sigma^+(v^+ = 1, N^+) + e^- \geq$. The electric dipole matrix elements that have been deduced from our PADs in the previous section, along with the requisite angular momentum machinery,² can provide predictions of ion angular momentum alignment and fully three-dimensional PADs. Aside from photoelectron spin polarization (which is expected to be negligible in this experiment), these predictions

completely describe the system state following photoionization. In this sense, the observation of the rotationally resolved PADs for this system constitutes a "perfect experiment."¹³

The $A^2\Sigma^+(3s\sigma)$ state of NO is the first member of the $ns\sigma$ Rydberg series. A Mulliken analysis of an *ab initio* calculation of the Rydberg electron orbital reveals 94% s ($l = 0$) character and 5.4% d ($l = 2$) character.¹⁴ In the central field (atom-like) approximation mostly p -wave ($l = 1$) and some f -wave ($l = 3$) character would be expected in an ionizing electric dipole transition. Although the observation of $\Delta N = \pm 1$ transitions demonstrates the presence of even- l waves in the departing photoelectron, their contribution is not very large (see Table III). Their presence would indicate the contribution of an additional dipolar interaction between the scattering photoelectron and the molecular ion. Perhaps more surprising is the considerable magnitude of the f -wave component. This contribution cannot be explained simply by the d -character of the Rydberg electron being channeled preferentially into the $l + 1$ rather than the $l - 1$ continua. Instead, it must arise from the scattering of the ejected electron caused by interaction with the quadrupole moment of the molecular core; or, in time-independent terms, it is caused by a mixing of the p and f continua by the ionic quadrupole moment.

In previous work^{1,5} we performed a fit to PADs resulting from $(1 + 1')$ REMPI via the $P_{21} + Q_1(25.5)$ transition to the $v_i = 0$ level of the $A^2\Sigma^+$ state of NO. Table III shows the results of the fit to this $v_i = 0$ data as well as to the $v_i = 1$ data. There is overall close agreement between the two fits; this result is a reflection of the fact that the PADs reported in Ref. 1 are quite similar to those reported in this work. This agreement helps confirm the prediction¹⁵ that the photoionization dynamics of the $A^2\Sigma^+$ state have only a weak dependence on the internuclear separation R of the NO^+ core. On closer inspection, there are some differences: in particular, the parameters Γ_f and $\delta_{d\sigma-d\pi}$ differ by more than the sum of their 1σ error bars. These discrepancies may be due, at least in part, to the "satellite peak" artifact of the data of Ref. 1. This artifact was caused by photoelectrons scattering off the wall of the flight tube into the detector, and amounts to a small blurring of the angular resolution. The addition of an electron baffle in our apparatus has almost completely suppressed this artifact (see Fig. 3).

Table III also shows the results of the frozen-core *ab initio* calculation performed by Rudolph and McKoy⁶ of these same electric dipole matrix elements. We have previously reported rather close agreement between those results and our analysis of data recorded following REMPI via the $v_i = 0$ level of the $A^2\Sigma^+$ state of NO.^{1,5} Our analysis of the $v_i = 1$ data reported here again shows close agreement with this *ab initio* calculation. This agreement helps to further confirm the prediction of the weak R dependence of the dynamics, as reported in Ref. 16. The strongest disagreement between experiment and theory is in the amount of parallel character for the ionizing transition, especially for the well-characterized p wave. Reference 6 predicts the p wave to be largely perpendicular in character; this, however, would yield much larger $|\Delta N| = 2$ contributions to the to-

TABLE IV. Predictions of ion state multipoles $T(K^+, Q^+)$ following $(1 + 1')$ REMPI via the $P_{21} + Q_1(22.5)$ transition to the $A^2\Sigma^+$ ($v_i = 1, N_i = 22$) level for $\Theta_T = 0^\circ$, $\Theta_T = 90^\circ$, and $\Theta_T = 54.7^\circ$. The $T(K > 0, Q)$ are divided by $T(0,0)$ for each combination of ΔN and Θ_T . The $T(0,0)$ are normalized such that $T(0,0) \equiv 100$ for $\Delta N = 0$, $\Theta_T = 0^\circ$. The values in parentheses represent 1σ uncertainties. The calculated values of $T(K, Q)$ [from Eqs. (8) and (9) of Ref. 2] for the intermediate state rotational level $N_i = 22$ are shown for comparison.

Θ_T	$T(K^+, Q^+)$	ΔN					$T(K, Q)$ $N_i = 22$
		-2	-1	0	+1	+2	
0°	$T(0,0)$	10.0(1.0)	3.5(4)	$\equiv 100$	3.6(4)	10.0(1.1)	100
	$T(2,0)$	0.55(7)	0.39(9)	0.75(3)	0.34(9)	0.54(6)	0.7411
	$T(4,0)$	-0.14(4)	-0.24(3)	0.000(9)	-0.30(3)	-0.15(4)	0
90°	$T(0,0)$	12.7(1.6)	5.3(4)	100(3)	5.2(4)	12.6(1.6)	100
	$T(2,0)$	-0.48(7)	-0.53(4)	-0.375(16)	-0.57(5)	-0.49(7)	-0.3706
	$T(2, \pm 2)$	0.48(6)	0.49(4)	0.459(15)	0.49(4)	0.48(6)	0.4539
	$T(4,0)$	0.055(14)	0.080(11)	0.000(5)	0.104(11)	0.060(16)	0
	$T(4, \pm 2)$	-0.043(11)	-0.063(9)	0.000(4)	-0.082(9)	-0.048(13)	0
54.7°	$T(0,0)$	11.8(1.4)	4.7(4)	100(3)	4.7(4)	11.8(4)	100
	$T(2,0)$	-0.19(5)	-0.30(4)	0.000(14)	-0.34(4)	-0.20(5)	0
	$T(2, \pm 1)$	$\mp 0.40(5)$	$\mp 0.39(4)$	$\mp 0.433(14)$	$\mp 0.39(4)$	$\mp 0.41(5)$	∓ 0.4279
	$T(2, \pm 2)$	0.34(4)	0.37(3)	0.306(10)	0.37(3)	0.34(4)	0.3026
	$T(4,0)$	0	0	0	0	0	0
	$T(4, \pm 1)$	$\pm 0.062(16)$	$\pm 0.095(13)$	0.000(5)	$\pm 0.122(13)$	$\pm 0.068(18)$	0
	$T(4, \pm 2)$	-0.031(8)	-0.048(7)	0.000(3)	-0.061(6)	-0.034(9)	0

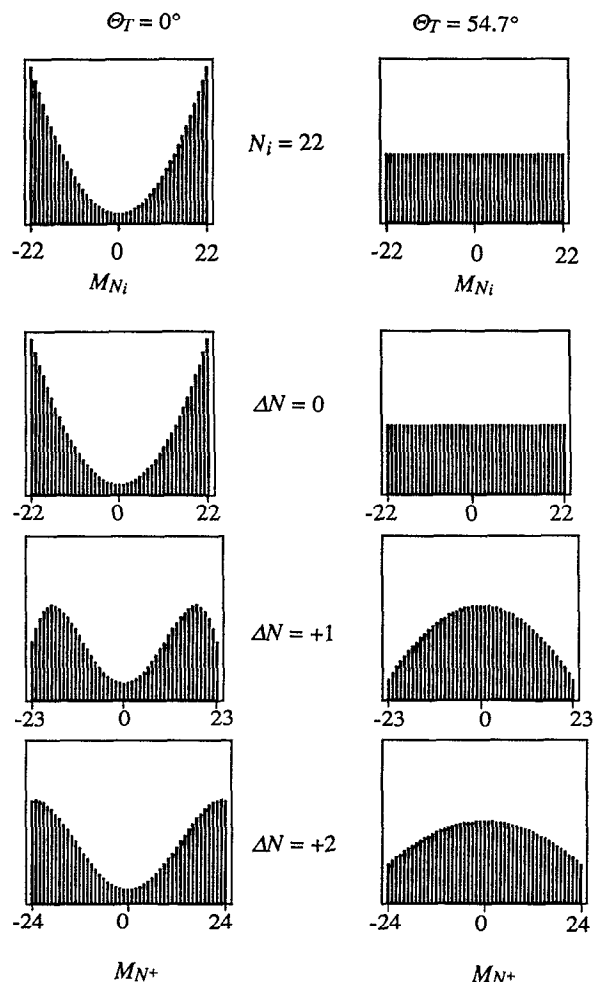


FIG. 8. Relative populations of the Zeeman sublevels (ρ_{M_i, M_i}) for $\Theta_T = 0^\circ$ and $\Theta_T = 54.7^\circ$, showing the M_{N_i} distribution for $N_i = 22$, and the M_{N^+} distributions for $N^+ = 22, 23$, and 24 . Coherences between sublevels are not represented. These distributions were calculated using the parameters listed in Table III.

tal cross section than observed experimentally.

An interesting feature of the data is the absence, within our detection limits, of $\Delta N = \pm 4$ transitions. Angular momentum constraints limit the maximum observable change in ion core rotation (i.e., ΔN) to $l + 1$ for each partial wave component l . For the dominant p wave, together with the $\Delta N + l = \text{odd}$ selection rule, this rule allows only $\Delta N = 0, \pm 2$. For the f wave, however, we can expect to see ΔN up to ± 4 . The fact that such large ΔN transitions are not observed is actually quite revealing because it helps determine the electric dipole transition matrix elements of the only two molecular-frame waves that can contribute to such transitions. Complete destructive interference between the $f\sigma$ and the $f\pi$ partial waves must be invoked to explain the absence of $\Delta N = \pm 4$ ionizing transitions. In addition, the relative magnitudes of the σ and π ($\lambda = 0$ and ± 1) components must be equal ($\Gamma_l = 1/3$) for complete cancellation to occur. Inclusion of the nonobservation of the large ΔN transitions in the fit greatly reduced the uncertainty of the adjustable parameters.

Another manifestation of the same effect is apparent when we compare the intensity of the $\Delta N = 0$ transition with that of the $\Delta N = \pm 2$. Our experiment reveals that the interference between the scattering of the $p\sigma$ and $p\pi$ components of the partial wave results in a shift of intensity from $\Delta N = \pm 2$ to $\Delta N = 0$. Since the p wave dominates the partial wave expansion, this shift results in about 75% of the ions being formed in a single N^+ rotational level! If the $p\sigma$ wave had been 180° out of phase from the $p\pi$ wave, rather than nearly in phase as our analysis revealed, then less than half of the ions would have been formed via a $\Delta N = 0$ transition. Because the various λ components of an l wave often have little or no relative phase shift (especially high- l waves that have little overlap with the molecular core), this effect is fairly widespread in molecular photoionization. This effect was first mentioned by Lynch *et al.*¹⁶ They explained how

the interference between $d\sigma$ and $d\pi$ partial waves suppresses the $\Delta J = \pm 3$ channels in the $(3 + 1)$ photoionization of H_2 via the $B^1\Sigma_u^+$ state. The effect has also been observed in this laboratory in rotationally resolved TOF-PES spectra of REMPI via the $E^2\Sigma^+(4s\sigma-3d\sigma)$ state of NO.¹⁷ In this case, despite a large contribution to the scattering photoelectron wave function from $f\lambda$ waves,¹⁸ no $\Delta N = \pm 4$ transitions were observed. In addition, laser-induced fluorescence measurements of rotational state distributions of HBr^+ ions formed by REMPI via $5p\pi$ Rydberg states¹⁹ show the absence of ionizing transitions with the maximum change of rotational quantum number that could be associated with the escape of a d wave. Since in this case a d wave is almost certainly present, this absence must also be attributed to interference between the $d\lambda$ components.

The parameters listed in Table III provide a complete description of the photoionization-scattering process. Consequently, we can make predictions of unobserved quantities such as ion alignment and the ϕ dependence of the PADs.² Table IV presents state multipoles for the intermediate state and for the ion rotational levels formed in the ionization. Figure 8 shows the M_N populations for two excitation-ionization geometries. Overall, not much alignment change occurs in the ionization step, especially for the ions formed in the $\Delta N = 0$ transitions. For these $N^+ = 22$ ions, within the limits of uncertainty of the parameters determined from the fit, there is no change in the alignment! One explanation of

this result is to consider the photoionization as an atom-like transition into the $|p\lambda\rangle$ continua followed by a scattering collision between the ion and the ejected photoelectron. The $\Delta N = 0$ channel would represent elastic scattering, which is unlikely to exchange angular momentum alignment between the fragments. The $\Delta N \neq 0$ channels would represent inelastic scattering, with the corresponding angular momentum transfer between the ion core and the photoelectron contributing to a change in alignment. This rationale is supported by the relatively large alignment change in $\Delta N = \pm 1$ ions, since such ions are formed entirely by the ejection of s and d waves.

Table V presents β_{LM} coefficients of the PADs [see Eq. (1)] predicted by the model via Eq. (6) of Ref. 2. In addition to directly giving us the shapes and intensities of the PADs (and thus the fully three-dimensional differential scattering cross sections), these quantities are state multipoles for the photoelectron orbital angular momenta, which are analogous to the $T(K, Q)$ of Table IV. Figure 9 displays predictions of the θ dependence of the PADs for $\phi = 0^\circ$ and 90° .

In essence, we have presented a quantum mechanically complete state-to-state "reaction." The photon and the intermediate state both have well-defined angular momenta (including alignment) and energies; we directly observe the center-of-mass momenta of the scattering photoelectron-ion system; we indirectly observe the vibrational and rotational

TABLE V. Predictions of the PAD coefficients β_{LM} [see Eq. (1)] following $(1 + 1')$ REMPI via the $P_{21} + Q_1(22.5)$ transition to the $A^2\Sigma^+(v = 1, N = 22)$ level for four values of Θ_T . The β_{LM} ($L > 0$) are divided by β_{00} for each combination of ΔN and Θ_T , and the β_{00} are normalized such that $\beta_{00} \equiv 100$ for $\Delta N = 0$, $\Theta_T = 0^\circ$. The values in parentheses represent 1σ uncertainties.

Θ_T	β_{LM}	ΔN				
		-2	-1	0	+1	+2
0°	β_{00}	9.6(1.0)	3.4(4)	$\equiv 100$	3.7(4)	10.5(1.1)
	β_{20}	0.12(3)	0.59(6)	0.83(3)	0.60(6)	0.13(3)
	β_{40}	-0.183(13)	-0.094(14)	0.001(3)	-0.080(12)	-0.159(12)
$\pm 90^\circ$	β_{00}	12.1(1.5)	5.2(4)	100(3)	5.4(4)	13.2(1.6)
	β_{20}	0.21(4)	0.79(6)	0.84(3)	0.79(6)	0.21(4)
	$\beta_{2\pm 2}$	-0.144(15)	-0.022(6)	-0.0101(15)	-0.018(7)	-0.124(13)
	β_{40}	0.072(5)	0.031(5)	-0.0006(12)	0.028(4)	0.064(5)
	$\beta_{4\pm 2}$	-0.057(4)	-0.025(4)	-0.0005(10)	-0.022(3)	-0.050(4)
-54.7°	β_{00}	11.2(1.4)	4.7(4)	100(3)	4.8(4)	12.3(1.5)
	β_{20}	0.18(4)	0.74(6)	0.84(3)	0.74(6)	0.18(4)
	$\beta_{2\pm 1}$	$\pm 0.071(11)$	$\pm 0.135(12)$	$\pm 0.001(4)$	$\pm 0.124(11)$	$\pm 0.063(10)$
	$\beta_{2\pm 2}$	-0.103(11)	-0.017(5)	0.0067(10)	-0.013(5)	-0.088(10)
	β_{40}	0	0	0	0	0
	$\beta_{4\pm 1}$	$\pm 0.082(6)$	$\pm 0.037(5)$	$\pm 0.0007(13)$	$\pm 0.032(5)$	$\pm 0.072(5)$
	$\beta_{4\pm 2}$	-0.041(3)	-0.018(3)	-0.0003(7)	-0.0162(24)	-0.036(3)
$+54.7^\circ$	β_{00}	11.2(1.4)	4.7(4)	100(3)	4.8(4)	12.3(1.5)
	β_{20}	0.18(4)	0.74(6)	0.84(3)	0.74(6)	0.18(4)
	$\beta_{2\pm 1}$	$\mp 0.071(11)$	$\mp 0.135(12)$	$\mp 0.001(4)$	$\mp 0.124(11)$	$\mp 0.063(10)$
	$\beta_{2\pm 2}$	-0.103(11)	-0.017(5)	0.0067(10)	-0.013(5)	-0.088(10)
	β_{40}	0	0	0	0	0
	$\beta_{4\pm 1}$	$\mp 0.082(6)$	$\mp 0.037(5)$	$\mp 0.0007(13)$	$\mp 0.032(5)$	$\mp 0.072(5)$
	$\beta_{4\pm 2}$	-0.041(3)	-0.018(3)	-0.0003(7)	-0.0162(24)	-0.036(3)

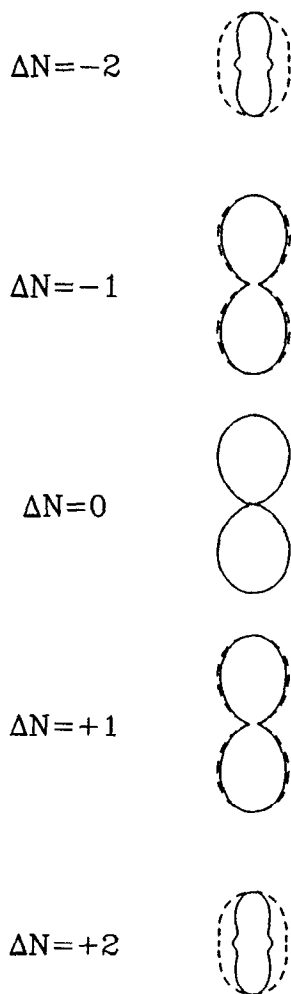


FIG. 9. Calculated ϕ dependence of the PADs for $(1 + 1')$ REMPI of NO via the $P_{21} + Q_1(22.5)$ transition to the $A^2\Sigma^+(v_i = 1, N_i = 22)$ level, with $\Theta_T = 90^\circ$. The solid line indicates the predicted θ dependence for $\phi = 0^\circ$ (XZ plane), and the dashed line shows the θ dependence for $\phi = 90^\circ$ (YZ plane).

state distribution of the ion via the measurement of the kinetic energies of the photoelectrons; and, within the limits of the model and the accuracy of our fit, we can calculate the photoelectron and ion angular momenta (again including alignment). Although we make no observation of the photoelectron spin polarization, the photoelectrons are expected to be almost completely unpolarized because of the very high degree of spin uncoupling in this system.

Finally, we must discuss two important limitations of this model. First, the model is a time-independent treatment of photoionization. It makes no comment on time-dependent phenomena (although it implicitly includes them), such as the possible role of vibrationally autoionizing resonances. There is, however, no reason to believe that vibrational autoionization is important in this system at the photoionization energies we have studied. Second, and more important, the model assumes that one set of parameters can describe the scattering of the photoelectron into channels that belong to different values of N^+ , despite corresponding differences in the photoelectron energy. In other words, the electric dipole transition matrix elements that connect the intermediate state to the $|\mathcal{A}\rangle$ continua are assumed to be energy independent. This assumption is supported by the *ab initio* work of Rudolph *et al.*¹⁵ which indicates that the ma-

trix elements have a relatively insensitive dependence on the photoelectron kinetic energy. A result of this assumption is that, in the high N limit, the model predicts symmetric intensities and shapes of the PADs that correspond to transitions involving the same absolute value of ΔN . If, however, one or more of the $|\mathcal{A}\rangle$ channels has a strong energy dependence, perhaps from a shape resonance, then this approximation breaks down, and asymmetric PADs would result. We have observed such asymmetries in our data with respect to the relative intensities of $\Delta N = \pm 1$ or $\Delta N = \pm 2$ transitions. This asymmetry is especially clear in Figs. 4 and 5, which show a systematic discrepancy between the model fit and the data: the $\Delta N < 0$ data are predicted to be more intense than observed; the opposite is true for the $\Delta N > 0$ data. Although it is possible that these asymmetries are an experimental artifact caused by kinetic energy discrimination of our photoelectron spectrometer, we consider it unlikely that we collect slower photoelectrons with a higher detection efficiency. We speculate, then, that this discrepancy between theory and experiment may result from the partial breakdown of the assumption of the invariance of the dipole matrix elements with respect to kinetic energy. It would be interesting to see if this speculation is borne out by theoretical calculations that include the photoelectron kinetic energy differences that correspond to the different ΔN photoionization channels.

CONCLUSIONS

Rotationally resolved photoelectron angular distributions (PADs) have been recorded following two-color REMPI via the $P_{21} + Q_1(22.5)$ transition to the $v_i = 1, N_i = 22$ level of the NO $A^2\Sigma^+$ Rydberg state. Reflection symmetry is observed to be broken [$I(\theta, \phi) \neq I(-\theta, \phi)$] when the angle between the polarization vectors of the two light beams is 54.7° . The rotationally resolved PADs recorded at a few excitation-ionization geometries ($\Theta_T = 0^\circ, \pm 54.7^\circ$, and 90°) hold sufficient dynamical information to provide a quantitative description of the photoionization process. A fit of electric dipole matrix elements was made using a model previously presented.^{1,2} The results of the fit are in close qualitative agreement with those of an earlier measurement^{1,5} and also with the results of an *ab initio* calculation⁶ for the same process (see Table III). A systematic discrepancy exists, however, between the model fit and the data: the observed intensities of $\Delta N = \pm 1$ and ± 2 peaks show an asymmetry that is not compatible with the constraints of the model.

For this (spin-uncoupled) system, the measurement of rotationally resolved PADs provides enough information to be regarded as a perfect experiment. Virtually all photoelectron and ion system state quantities, namely, ion state distributions, fragment momenta, and alignment of fragment angular momenta, have been deduced from these parameters. Although we do not present an observation of photoelectron spin polarization, virtually none is expected to arise in this experiment. Thus, the detailed information in rotationally resolved photoelectron angular distributions following molecular REMPI provides a complete description of the photoionization dynamics.

ACKNOWLEDGMENTS

K.L.R. thanks the SERC for a NATO postdoctoral fellowship. We are grateful to Jinchun Xie and Sarah Allendorf for useful discussions. We acknowledge the support of the U.S. Air Force Office of Scientific Research under Contract No. AFOSR 89 0264 and from the National Science Foundation under Grant No. PHY-9020457.

¹ S. W. Allendorf, D. J. Leahy, D. C. Jacobs, and R. N. Zare, *J. Chem. Phys.* **91**, 2216 (1989).

² K. L. Reid, D. J. Leahy, and R. N. Zare, *J. Chem. Phys.* **95**, 1746 (1991).

³ S. N. Dixit and V. McKoy, *J. Chem. Phys.* **82**, 3546 (1985).

⁴ K. S. Viswanathan, E. Sekreta, E. R. Davidson, and J. P. Reilly, *J. Phys. Chem.* **90**, 5078 (1986).

⁵ K. L. Reid, D. J. Leahy, S. W. Allendorf, and R. N. Zare, in *Resonance Ionization Spectroscopy, 1990* (Institute of Physics, Bristol, 1991). Please note that the $M = \pm 1$ terms have been neglected in this reference. Accordingly, in this reference Fig. 2 is in error.

⁶ H. Rudolph and V. McKoy, *J. Chem. Phys.* **91**, 2235 (1989).

⁷ The corrected intensity $I(t) = I_0(t) / [1 - (1/N) \int_0^t I_0(t') dt']$, where N = total number of laser shots and $I_0(t) dt$ is the uncorrected number of counts arriving in the time interval $t, t + dt$.

⁸ K. Blum, *Density Matrix Theory and Applications* (Plenum, New York, 1981); R. N. Zare, *Angular Momentum* (Wiley, New York, 1988).

⁹ W. H. Press, B. P. Flannery, S. A. Teukolsky, and W. T. Vetterling, *Numerical Recipes* (Cambridge University, Cambridge, England, 1986), pp. 523–528.

¹⁰ P. H. Vaccaro (private communication).

¹¹ S. N. Dixit, D. L. Lynch, V. McKoy, and W. M. Huo, *Phys. Rev. A* **32**, 1267 (1985).

¹² J. Xie and R. N. Zare, *J. Chem. Phys.* **93**, 3033 (1990).

¹³ J. Kessler, *Comments At. Mol. Phys.* **10**, 47 (1981); H. Klar and H. Kleinpoppen, *J. Phys. B* **15**, 933 (1982).

¹⁴ H. Rudolph, S. N. Dixit, V. McKoy, and W. M. Huo, *J. Chem. Phys.* **88**, 1516 (1988).

¹⁵ H. Rudolph, V. McKoy, and S. N. Dixit, *J. Chem. Phys.* **90**, 2570 (1989).

¹⁶ D. L. Lynch, S. N. Dixit, and V. McKoy, *Chem. Phys. Lett.* **123**, 315 (1986).

¹⁷ D. J. Leahy (unpublished results).

¹⁸ H. Rudolph and V. McKoy, *J. Chem. Phys.* **93**, 7054 (1990).

¹⁹ J. Xie and R. N. Zare, *Chem. Phys. Lett.* **159**, 399 (1989).